

# Coherent total internal reflection dark-field microscopy: label-free imaging beyond the diffraction limit

Philipp von Olshausen<sup>1,2</sup> and Alexander Rohrbach<sup>1,2,\*</sup>

<sup>1</sup>Laboratory for Bio- and Nano-Photonics, Department of Microsystems Engineering—IMTEK, University of Freiburg, 79110 Freiburg, Germany

<sup>2</sup>Centre for Biological Signaling Studies (BIOS), University of Freiburg, 79110 Freiburg, Germany

\*Corresponding author: rohrbach@imtek.de

Received June 13, 2013; revised August 13, 2013; accepted September 9, 2013;

posted September 11, 2013 (Doc. ID 192187); published October 7, 2013

Coherent imaging is barely applicable in life-science microscopy due to multiple interference artifacts. Here, we show how these interferences can be used to improve image resolution and contrast. We present a dark-field microscopy technique with evanescent illumination via total internal reflection that delivers high-contrast images of coherently scattering samples. By incoherent averaging of multiple coherent images illuminated from different directions we can resolve image structures that remain unresolved by conventional (incoherent) fluorescence microscopy. We provide images of 190 nm beads revealing resolution beyond the diffraction limit and slightly increased object distances. An analytical model is introduced that accounts for the observed effects and which is confirmed by numerical simulations. Our approach may be a route to fast, label-free, super-resolution imaging in live-cell microscopy. © 2013 Optical Society of America

OCIS codes: (180.0180) Microscopy; (070.6110) Spatial filtering; (030.1670) Coherent optical effects; (290.0290) Scattering.

<http://dx.doi.org/10.1364/OL.38.004066>

Usually the interference of light coherently scattered at different object structures deteriorates image quality. Using fluorescence microscopy in scattering media the interference effects of the coherent excitation light lead to unwanted excitation patterns. These intensity artifacts can vary by up to 100% of the illumination intensity [1] and often remain undiscovered, also because the convolution with the point-spread function (PSF) blurs the image including all artifacts.

Whereas fluorescence-based techniques are subject to photobleaching, techniques based on coherent scattering, such as, e.g., digital holography [2] and synthetic aperture microscopy [3], do not need any labeling and have been applied for imaging albeit with limited resolution. Others have used coherent structured illumination to reconstruct an enlarged field spectrum of the object but these approaches require complicated numerical postprocessing and they did not show the separation of objects below the 1  $\mu\text{m}$  scale [4,5]. Recently, very high lateral resolution has been shown in coherent imaging using a holographic detection scheme [6]. However, this approach uses two opposing objective lenses and extensive postprocessing, which makes its application cumbersome.

Although still visible, coherence artifacts are reduced by total internal reflection (TIR) microscopy, which is mainly used in fluorescence mode, known as TIRF [7]. TIR can also be combined with dark-field (DF) detection to enhance contrast. However, this has only been used for single particle tracking [8,9].

Here, we present an implementation of coherent imaging that combines evanescent illumination via TIR with DF microscopy and which yields images of scattering samples near the coverslip with a lateral resolution beyond the diffraction limit. It does not require any labeling of the sample as coherently scattered light is exploited, which is generated by the refractive index

inhomogeneities of the sample. The evanescent illumination assures strong axial sectioning and excellent contrast which is further improved by the DF detection scheme.

To obtain one TIR-DF image we acquire many coherent images with evanescent illumination from different directions which are then incoherently superposed. This simple approach is able to resolve objects that remain unresolved by conventional TIRF (fluorescence) microscopy. The increased resolution comes at the cost of slight distortion artifacts. We also present an analytical model describing the observed imaging effects, which we confirm using numerical simulations.

The experimental setup is shown in Fig. 1. A collimated, linearly polarized 488 nm laser beam (2214-20SL, JDSU, USA) illuminates a reflective spatial light modulator [(SLM) LCR-2500, Holoeye Photonics, Germany]. Holograms displayed on the SLM act as diffractive phase

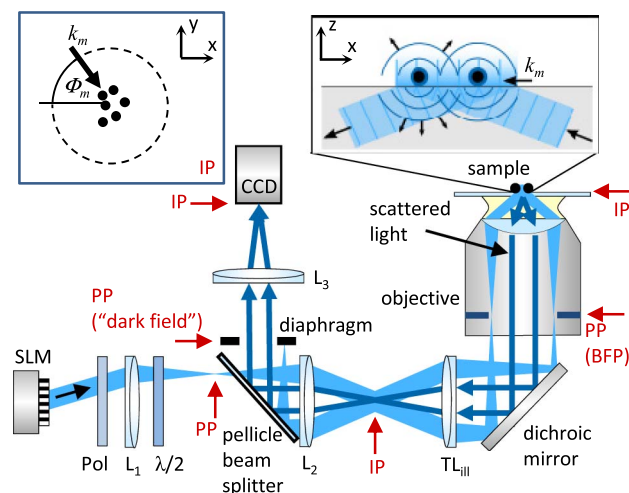


Fig. 1. Scheme of the experimental setup.

gratings that deflect the beam. The lens  $L_1$  focuses the beam into the pupil plane (PP). A polarization filter (Pol) and a motorized half-wave plate ( $\lambda/2$ ) are used to assure a high degree of s-polarization with respect to the coverslip-sample interface for all illumination directions. A 4f-system consisting of the lens  $L_2$  and the illumination tube lens  $TL_{\text{ill}}$  images the focus from the PP into the outermost ring of the back focal plane (BFP) of an objective lens (HCX PL Apo, 100 $\times$ , NA 1.46, oil immersion, Leica, Germany) with high NA. This results in a plane wave emanating from the objective lens under such a high angle that it undergoes TIR at the interface between the glass coverslip and the sample in watery solution. The resulting evanescent wave at the interface illuminates a thin section of the sample and decays exponentially in axial  $z$ -direction. Blazed grating phase holograms on the SLM are used to change the azimuthal direction  $\phi_m$  of the evanescent wave illumination. This means that the real part of the  $k$ -vector of the evanescent field rotates in the sample plane (= image plane, IP). The reflected light as well as some of the light scattered by the sample is collected by the objective lens. A 92/8-pellicle beam splitter (BP 108, Thorlabs GmbH, Germany) reflects 8% of this light out of the beam path. This makes a PP (marked "dark field") accessible without interfering with the illumination beam path. In this plane a diaphragm blocks all TIR light and by this constitutes DF conditions. Only the scattered light (same wavelength, shown in dark blue for better visibility) passes the diaphragm and the lens  $L_3$  and forms an image on a CCD camera (GC 1350, Allied Vision Technologies, Canada).

As the mirror below the objective lens is implemented as a dichromatic beam splitter we can also acquire fluorescence images with a different detection beam path and CCD camera (not shown). Additionally, this setup allows doing structured illumination microscopy in fluorescence mode (TIRF-SIM) with a lateral resolution of about 100 nm [10,11]. These techniques serve as a reference for the performance of TIR-DF microscopy.

We acquired  $N = 72$  partial images each illuminated from a different direction and generated by a different coherent scattering process. The intensities of the coherent images are averaged to yield the final (radially coherent and tangentially incoherent) TIR-DF image.

For each partial image the object near the coverslip is illuminated by an evanescent wave incident from the azimuthal direction  $\phi_m$ . The  $m$ th electric field reads  $E_m(r, z) = E_0 e^{-z/d_{pd}} e^{-ik_m r}$  ( $m = 1 \dots N$ ). Here,  $r$  denotes the lateral position in the  $x$ - $y$  plane,  $z$  refers to the axial direction, and  $d_{pd}$  is the 1/e-penetration depth of the evanescent field. The amplitude  $E_0$  will be neglected in the further discussion as well as the axial decay of the illumination intensity. Instead the imaging will be treated in 2D, which is well suited for TIR techniques.  $k_m = 2\pi n_i \sin(\theta_i) / \lambda_0 \cdot [-\cos(\phi_m) e_x + \sin(\phi_m) e_y]$  is the real part of the  $k$ -vector of the evanescent field, where  $n_i = 1.52$  is the refractive index of the medium,  $\lambda_0 = 488$  nm the vacuum wavelength, and  $\theta_i \approx 67^\circ$  the polar angle of incidence.  $k_m$  is perpendicular to the illuminating wavefronts and its azimuthal direction  $\phi_m$  is evenly varied from  $0^\circ$  to  $360^\circ$  for all  $N$  images. The

corresponding wavelength of the evanescent field is  $\lambda_{ev} = \lambda_0 / [n_i \cdot \sin(\theta_i)] \approx 350$  nm.

One partial image  $I_m(r)$  of the object distribution  $f(r)$  with incident field  $E_m(r) \approx e^{-ik_m r}$  is then described by  $I_m(r) = |f(r) \cdot E_m(r, \phi_m) \otimes h_c(r)|^2$ , where  $h_c(r)$  is the coherent PSF and  $\otimes$  denotes convolution. The final TIR-DF image, averaged over multiple, symmetrically distributed illumination directions  $\phi_m = 360^\circ / N \cdot m$  is given by  $I_{\text{final}}(r) = 1/N \cdot \sum_{m=1}^N I_m$  and can be written as

$$I_{\text{final}}(r) = \frac{1}{N} \sum_{m=1}^N |f(r) \cdot E_m(r, \phi_m) \otimes h_c(r)|^2. \quad (1)$$

Approximating the object distribution  $f(r) = \sum_j f_j(r)$  as a sum of point scatterers  $f_j(r) = \delta(r - r_j)$ , which is well suited for small beads, and applying the law of distributivity, leads to

$$\begin{aligned} I_{\text{final}}(r) &= \frac{1}{N} \sum_{m=1}^N \left| \left[ \sum_j f_j(r) \right] \cdot E_m(r, \phi_m) \otimes h_c(r) \right|^2 \\ &= \frac{1}{N} \sum_{m=1}^N \left| \sum_j \underbrace{(f_j(r) \cdot E_m(r, \phi_m)) \otimes h_c(r)}_{F_{m,j}(r, \phi_m)} \right|^2, \end{aligned} \quad (2)$$

where  $F_{m,j}(r, \phi_m)$  is the (electric) field image of the  $j$ th scatterer under illumination with  $E_m(r, \phi_m)$ . Generally speaking,  $F_{m,j}$  is a complex function and can thus be expressed as  $F_{m,j}(r, \phi_m) = |F_{m,j}(r, \phi_m)| \cdot \exp[-i\varphi(r, \phi_m)]$ , where  $\varphi(r, \phi_m)$  is the phase of the field image that depends on the position  $r$  of the scatterer and the direction of illumination  $\phi_m$ . Expansion of the multifield interference of Eq. (2) thus yields

$$\begin{aligned} I_{\text{final}} &= \frac{1}{N} \sum_{m=1}^N \left[ \sum_j |F_{m,j}|^2 \right. \\ &\quad \left. + \sum_{j \neq k} 2 |F_{m,j}|^2 \cdot |F_{m,k}|^2 \cdot \cos(\varphi_{m,j} - \varphi_{m,k}) \right]. \end{aligned} \quad (3)$$

Here, dependencies were neglected for clarity. A second index  $k$  was introduced to distinguish the local phase of scatterer  $j$  and scatterer  $k$ . For point scatterers the amplitude  $|F_{m,j}(r, \phi_m)|$  does actually not depend on the direction of illumination, so that Eq. (3) can be further simplified to

$$\begin{aligned} I_{\text{final}} &= \sum_j |F_j|^2 \\ &\quad + \frac{2}{N} \sum_{j \neq k} |F_j|^2 \cdot |F_k|^2 \cdot \sum_{m=1}^N \underbrace{\cos(\varphi_{m,j} - \varphi_{m,k})}_{\Delta\varphi_{mjk}}. \end{aligned} \quad (4)$$

The first term of Eq. (4) represents the incoherent image of the object. The second term sums the phase differences  $\Delta\varphi_{mjk}$  between pairwise point scatterers over all illumination directions weighted with a cosine. This sum is generally not zero but depends crucially on the locations  $r$  of the scatterers  $j$  and  $k$  and on the direction

of illumination  $\phi_m$ . Equation (4) will help to describe and understand the observed effects in the final image, as presented further down.

We imaged 190 nm fluorescent polystyrene beads, which were air-dried and then reimmersed in deionized water, to quantify the performance of TIR-DF microscopy and compare it to conventional TIRF. Additionally, we used TIRF-SIM to verify the exact positions of all the single beads (images not shown).

Figures 2(a)–2(c) show coherent partial images of 190 nm beads for three different directions  $\phi_m$  of TIR illumination. The images exhibit strong interferences typical for coherent imaging. They do not allow to identify any beads and differ significantly for the various illumination directions. Two regions of interest (ROI) are highlighted to illustrate the effects of an oblique, directional, coherent illumination and its influence on the final image. A magnified and autoscaled version of the ROIs is given in Fig. 2(d), including the final TIR-DF image.

ROI-1 shows two neighboring beads at a distance of  $d = 156$  nm (from TIRF-SIM). Their appearance in the partial images strongly depends on the direction of illumination. This can be understood on the basis of coherent image formation. In Fig. 2(b), the two beads are illuminated along their connecting axis. As their distance is about half the wavelength of the evanescent field they are illuminated and thus scattering coherently with a phase difference of  $\Delta\phi_{mjk} = \pi$ . Consequently, their electric field images  $E_m(x)$  are out of phase. This results in a final intensity image, which shows the two beads at full contrast, albeit at a slightly increased bead distance  $d_{\text{mes}} > d$ . This process of image formation is schematically illustrated in the orange-framed inset with the wavefronts shown in gray and the two beads, drawn as point scatterers, shown in red and blue.

In Fig. 2(c), the same two beads are illuminated perpendicular to their connecting axis. This results in

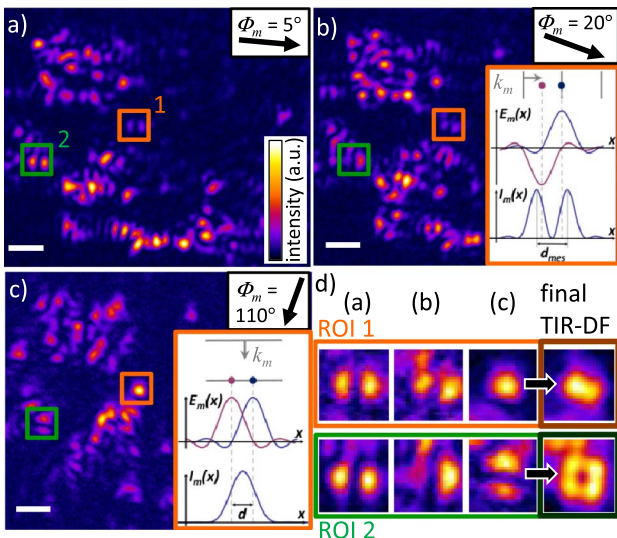


Fig. 2. Coherent partial images of 190 nm beads with evanescent wave illumination from different directions, (a) 5°, (b) 20°, and (c) 110°. The insets illustrate the formation of a coherent image of two point scatterers as in ROI 1. (d) Magnified view on the ROIs 1 and 2, including the final TIR-DF image. Scale bar is 1  $\mu\text{m}$ .

an in-phase scattering ( $\Delta\phi_{mjk} = 0$ ) and thus in in-phase field images  $E_m(x)$ , as indicated in the orange-framed inset. The resulting intensity image  $I_m(x)$  shows only a single peak at the center of the beads so that they cannot be separated at all. In Fig. 2(a), the direction of illumination is only slightly different than in Fig. 2(b). Thus, the corresponding change in  $\Delta\phi_{mjk}$  is small, which results in a similar image, as can be seen in Fig. 2(d).

The same principle, namely that the direction of coherent illumination determines the image of neighboring structures due to different phase relations of the scatterers, holds true for the cluster of four beads shown in ROI-2 in Fig. 2. As these four beads are at distances of about 200 nm (again about half the illumination wavelength), an out-of-phase illumination ( $\Delta\phi_{mjk} = \pi$ ) results in high separation contrast. Remarkably, in the final TIR-DF image all four beads are well resolved, as shown in Fig. 2(d).

Figure 3(a) compares a conventional TIRF image (b) to the complete final TIR-DF image (a). In TIR-DF mode, all beads and bead clusters are well reproduced in position and shape. Clusters of several beads appear slightly “blown up” in size but the single beads are significantly better resolvable than in the conventional TIRF image. These effects can be even better seen in the magnified images of the green-framed ROI shown in Figs. 3(c) and 3(d).

Figures 3(g) and 3(h) show two line profiles to quantify the effects of TIR-DF imaging. Figure 3(g) shows the diagonal line profile of the cluster of four beads. Whereas the beads cannot be separated by conventional TIRF, in TIR-DF they can clearly be resolved. The peak-to-peak distance in TIR-DF is 323 nm, which is an approximately 23% increase compared to their real distance (263 nm from TIRF-SIM). In Fig. 3(h), the line profile of a cluster

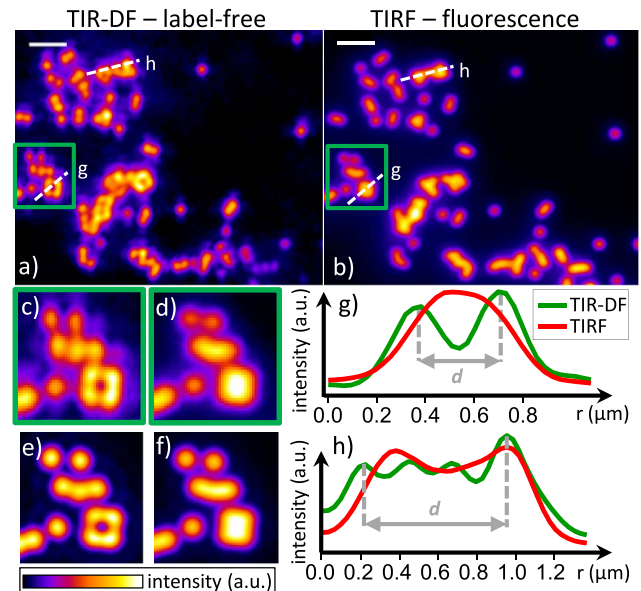


Fig. 3. 190 nm beads imaged by (a) TIR-DF and (b) TIRF microscopy. Scale bar is 1  $\mu\text{m}$ . (c) and (d) Magnified view of the green-framed ROI in (a) and (b), respectively. (e) and (f) Numerical simulation of TIR-DF and TIRF imaging, respectively, of the bead distribution as in the ROI. (g) and (h) Line profiles as marked in subfigures (a) and (b).

of several beads is shown. Here, TIR-DF reveals beads in the central area of this cluster which are not resolvable by conventional TIRF. The distance between the two outermost peaks of four neighboring beads is 724 nm in TIR-DF instead of 642 nm (13% increase). However, the beads can be clearly resolved in TIR-DF.

TIR-DF can resolve closer objects than conventional TIRF microscopy but the images exhibit larger distances between these objects. These effects are a result of the averaging over many images with coherent illumination from various directions. The phase relations between objects vary with the illumination, which leads to different coherent partial images. The averaging process partly maintains the high contrast from local phase differences  $\Delta\varphi_{mjk} = \pi$ , but also partly the increased distance. These two effects are also represented in Eq. (4), where the first term represents an incoherent image and the second term superimposes the coherent interferences. This latter term represents the observed effects of enlarged bead-to-bead distances at increased contrast. It should be mentioned that only neighboring structures influence each other significantly as the coherent field PSFs drop quite rapidly.

To approve our analytical model of the imaging process we performed 2D numerical simulations of the imaging of a distribution of beads almost identical to the one in Figs. 3(c) and 3(d). As can be seen in Figs. 3(e) and 3(f) the simulated images coincide well with the experimental results and thus confirm our analytical model of image formation in TIR-DF microscopy.

For practical reasons, simulations were performed in Fourier space. The conventional TIRF image was calculated as

$$I_{\text{TIRF}}(r) = |FT^{-1}\{\tilde{F}_I(k) \cdot H_I(k)\}|, \quad (5)$$

where  $\tilde{F}_I(k)$  is the image intensity spectrum and  $H_I(k)$  is the incoherent optical transfer function. The TIR-DF image was calculated as

$$I_{\text{TIR-DF}}(r) = \frac{1}{N} \sum_{m=1}^N |FT^{-1}\{\tilde{F}_C(k) \cdot H_C(k + k_m)\}|^2, \quad (6)$$

where the inclined illumination is accounted for by a shifted coherent optical transfer function  $H_C(k + k_m)$

with  $k_m$  being the real part of the wave vector of the evanescent illumination.  $\tilde{F}_C(k)$  is the object's field spectrum. Equation (6) is equivalent to Eq. (1). The discretization was 17.5 nm in both lateral directions ( $x$  and  $y$ ). All other simulation parameters were chosen as in the experimental measurements, namely  $\lambda_0 = 488$  nm, detection NA = 1.33,  $\theta_i = 67^\circ$ , and  $N = 72$ .

TIR-DF microscopy is a simple, high-contrast TIR technique for the imaging of scattering structures close to the coverslip. It shows clearly increased resolution compared to conventional TIRF, albeit at the cost of slight image distortions. However, this straightforward technique is potentially very fast since all  $N$  images could be acquired during one exposure time of the camera, which can be just a few milliseconds. Thus, replacing the SLM by scan-mirrors, TIR-DF microscopy may be a route to fast, super-resolution imaging of dynamic structures in living cells without the need of any labeling.

This study was supported by the Excellence Initiative of the German Federal and State Governments (EXC 294). The authors thank C. Gohn-Kreuz for helpful discussions about the analytical model.

## References

1. A. Rohrbach, *Opt. Lett.* **34**, 3041 (2009).
2. W. M. Ash III and M. K. Kim, *Opt. Express* **16**, 9811 (2008).
3. M. Kim, Y. Choi, C. Fang-Yen, Y. Sung, R. R. Dasari, M. S. Feld, and W. Choi, *Opt. Lett.* **36**, 148 (2011).
4. S. Chowdhury, A.-H. Dhalla, and J. Izatt, *Biomed. Opt. Express* **3**, 1841 (2012).
5. B. Littleton, K. Lai, D. Longstaff, V. Sarafis, P. Munroe, N. Heckenberg, and H. Rubinsztein-Dunlop, *Micron* **38**, 150 (2007).
6. Y. Cotte, F. Toy, P. Jourdain, N. Pavillon, D. Boss, P. Magistretti, P. Marquet, and C. Depeursinge, *Nat. Photonics* **7**, 113 (2013).
7. D. Axelrod, *J. Cell Biol.* **89**, 141 (1981).
8. I. Braslavsky, R. Amit, B. M. J. Ali, O. Gileadi, A. Oppenheim, and J. Stavans, *Appl. Opt.* **40**, 5650 (2001).
9. S. Kim, P. C. Blainey, C. M. Schroeder, and X. S. Xie, *Nat. Methods* **4**, 397 (2007).
10. R. Fiolka, M. Beck, and A. Stemmer, *Opt. Lett.* **33**, 1629 (2008).
11. P. von Olshausen, H. J. Defeu Soufo, K. Wicker, R. Heintzmann, P. L. Graumann, and A. Rohrbach, *Biophys. J.* **105**, 1171 (2013).